bioRxiv preprint doi: https://doi.org/10.1101/2022.01.20.477166; this version posted January 22, 2022. The copyright holder for this preprint (which was not certified by peer review) is the author/funder. All rights reserved. No reuse allowed without permission.

Development and characterization of a human arteriovenous malformation (AVM)-on-a-chip model

Kayla Soon [1,2], Mengyuan Li [1,2], Ruilin Wu [1,3], Jason E. Fish [1,3,4,5], Sara S Nunes [1,2,3,5,*]

[1] Toronto General Hospital Research Institute, University Health Network, Toronto, Canada

[2] Institute of Biomedical Engineering, University of Toronto, Toronto, Canada

[3] Department of Laboratory Medicine and Pathobiology, University of Toronto, Toronto, Canada

[4] Peter Munk Cardiac Centre, University Health Network, Toronto, Canada

[5] Heart and Stroke/Richard Lewar Centre of Excellence, University of Toronto, Toronto, Canada

* Corresponding author:
Sara S. Nunes Vasconcelos
University Health Network,
101 College St. MaRS TMDT 3-904,
Toronto, ON, M5G 1L7
Canada.
Email address: sara.vasconcelos@utoronto.ca

bioRxiv preprint doi: https://doi.org/10.1101/2022.01.20.477166; this version posted January 22, 2022. The copyright holder for this preprint (which was not certified by peer review) is the author/funder. All rights reserved. No reuse allowed without permission.

Abstract

Brain arteriovenous malformations (AVMs) are a disorder where abnormal, enlarged blood vessels connect arteries directly to veins, without an intervening capillary bed. AVMs are one of the leading causes of hemorrhagic stroke in children and young adults. Most human sporadic brain AVMs are associated with genetic activating mutations in the KRAS gene. Our goal was to develop an *in vitro* model of human AVMs using human endothelial cells harbouring a clinically relevant KRAS mutation in a dynamic microfluidic culture system to enable vessel formation and perfusion to capture key morphological structure and barrier dysfunction characteristics of AVM. Using a combination of normal and KRAS4A^{G12V} mutated endothelial cells (ECs), we demonstrated that vessels formed by KRAS4A^{G12V} ECs were significantly wider and more leaky than vascular beds formed by wild-type ECs, recapitulating key structural and functional hallmarks of AVMs. Immunofluorescence staining revealed a breakdown of adherens junctions in mutant KRAS vessels only, leading to increased permeability of the vessel network. Furthermore, treatment with a MEK inhibitor, but not a PI3K inhibitor, resulted in an improvement in endothelial barrier function (decreased permeability) without affecting vessel width. Here, we have demonstrated the ability to create human KRAS-dependent AVM-like vessels *in vitro* in a self-assembling microvessel platform that is amenable to drug testing.

bioRxiv preprint doi: https://doi.org/10.1101/2022.01.20.477166; this version posted January 22, 2022. The copyright holder for this preprint (which was not certified by peer review) is the author/funder. All rights reserved. No reuse allowed without permission.

Introduction

Brain arteriovenous malformation (AVM) is an abnormal formation of blood vessels creating a direct connection between arteries and veins, which is characterized by high blood flow and vessel enlargement. Instead of a normal hierarchical vasculature, a tangle of vessels that lack the barrier integrity and the stability of normal capillary networks is formed. Individuals with AVMs are at increased risk of hemorrhage due to the direct shunting of high-pressure flow from the artery [1]. AVMs are responsible for 4% of all intracerebral haemorrhages and account for almost one third of them in young adults [2]. There are no pharmacological treatments for AVM. The only treatment options are surgical resection and embolization of small AVMs or stereotactic radiosurgery for inoperable vessels to reduce vessel size. Both procedures are highly invasive with a recurrent hemorrhage risk as high as 18% in the first year. Approximately one third of all AVM cases are untreatable with currently available options [3].

Various mutations in the mitogen-activated protein kinases (MAPK/RAS) pathway have been implicated in AVM pathology. Recently, somatic activating KRAS mutations in endothelial cells (ECs) have been reported in as many as 50% of clinical samples [4,5]. Nikolaev *et al.* [5] showed that somatic activating KRAS mutations in ECs derived from patient AVMs or introduced in human umbilical vein endothelial cells (HUVECs) led to increased ERK1/2 phosphorylation causing disruption of vascular endothelial (VE)-cadherin localization in adherens junctions. This is thought to increase the permeability of the vessel wall, and to leave vessels prone to hemorrhage [5,6]. Although these genetic mutations are sufficient for the development of AVM in zebrafish and mouse models [7], the initiation, development, and remodelling of these dynamic vessel malformations are influenced by factors in the microenvironment. Specifically, vascular endothelial growth factor (VEGF) and other pro-angiogenic factors are highly expressed in AVMs, leading to increased vessel permeability and susceptibility to rupture [8,9]. Other pathways, such as Notch and transforming growth factor (TGF)-β/bone morphogenetic protein (BMP) have also been implicated in AVM regulation [10], particularly with discontinuity of cell-cell junctions and cell proliferation, resulting in vascular dysplasia and instability [9,11,12]. Moreover, there is growing evidence suggesting that the AVM microenvironment may encourage AVM growth. Inflammation driven by local macrophages and reduction of

bioRxiv preprint doi: https://doi.org/10.1101/2022.01.20.477166; this version posted January 22, 2022. The copyright holder for this preprint (which was not certified by peer review) is the author/funder. All rights reserved. No reuse allowed without permission.

pericyte coverage have been described as contributory factors by promoting angiogenic responses [13,14]. Additionally, a high flow rate is a defining feature in AVMs that leads to a positive feedback loop to increase local vessel enlargement in high-velocity vessels [15]. Hovwever, there is limited knowledge as to how environmental cues from surrounding cells, hemodynamics, and the KRAS mutation contribute to the pathogenesis of AVMs.

Animal models of the disease have achieved variable degrees of success in generating vessel lesions with characteristics that match human pathology. Several transgenic mouse models of hereditary hemorrhagic telangiectasia (HHT), an inherited disease known to cause AVMs, involve genetic inhibition or deletion of either *Eng* or *Alk1* genes in combination with angiogenic induction to generate AVMs indiscriminately in various organs [16–18]. These models have shown vessel dilation, arteriovenous shunt, and hemorrhaging of vessel malformations. However, there was large intra and inter sample variability [19]. The incidence of observable AVMs can be low and there is often high and early mortality associated with these models [20,21]. Recently, mouse and zebrafish models with the $KRAS^{G12V}$ or $KRAS^{G12D}$ mutation displayed enlarged vessels [7,22]. These animal models have contributed to defining the mechanism of sporadic brain AVMs. However, validation and corroboration in human-relevant models has largely been limited to 2D monolayers [23].

In recent years, organ-on-a-chip models have emerged as candidates to address the limitations of 2D models and species-specific factors in disease modeling and drug development. In comparison to cell monolayers, organ-on-a-chip models have increased architectural complexity, mimicking key aspects of *in vivo* tissue physiology [24]. Using a combination of adjoining channels and interfaces, they enable precise spatiotemporal control of mechanical and chemical stimuli to probe tissue responses [25,26]. Several studies have successfully produced vessel-like networks using ECs from different origins, in combination with supporting cells such as fibroblasts [27,28], pericytes [29,30], or mesenchymal stem cells [31]. Self-assembled microvessels on-chip models are formed in the presence of media flow, allowing perfusion of the vasculature [32]. Rather than having predefined geometries, the self-assembling nature of microvasculature-on-a-chip forms an organic vasculature with vessels of varying shapes and sizes. This aspect is particularly relevant when studying diseases that lead to alterations in vessel diameter, such as in AVMs [26].

bioRxiv preprint doi: https://doi.org/10.1101/2022.01.20.477166; this version posted January 22, 2022. The copyright holder for this preprint (which was not certified by peer review) is the author/funder. All rights reserved. No reuse allowed without permission.

Our goal is to recapitulate the key hallmarks of AVMs *in vitro* using human ECs harbouring a clinically relevant KRAS mutation described in patients with sporadic AVMs in a microfluidic platform that allows 3D vessel assembly and perfusion. We also aim to test the impact of MEK inhibitors on AVM structural and functional parameters. We found that a mosaic culture of $KRAS^{G12V}$ mutant and wildtype ECs led to irregularly shaped and enlarged microvessels, with increased vessel wall permeability. Treatment with a MEK inhibitor restored barrier function but did not reverse vessel dilation.

bioRxiv preprint doi: https://doi.org/10.1101/2022.01.20.477166; this version posted January 22, 2022. The copyright holder for this preprint (which was not certified by peer review) is the author/funder. All rights reserved. No reuse allowed without permission.

Materials and Methods

2.1 Cells Culture

Immortalized (Im)-HUVECs (a gift from Dr. Roger Kamm at MIT) were grown in VascuLife VEGF Endothelial Medium (Lifeline Cell Technology). Im-HUVECs constitutively express green fluorescent protein (GFP) [33]. KRAS^{G12V} Im-HUVECs were grown in Endothelial Cell Medium (ScienCell). Normal human lung fibroblasts (NHLF; Lonza) were grown in DMEM (ThermoFisher) supplemented with 20% fetal bovine serum (FBS). NHLF of passage 5-7 were used in experiments. All cells were cultured in cell culture flasks coated with 1% gelatin until they reached 85-90% confluency.

2.2 KRAS4A^{G12V} HUVECs Transposon Mutagenesis

Telomerase-immortalized human umbilical vein endothelial cells (Im-HUVEC) and plasmid vectors were kindly provided by Dr. Joshua D. Wythe at the Baylor College of Medicine (United States). To generate the Im-HUVEC line that stably expresses KRAS^{G12V} proteins, 1.5µg of TetON-mScarlet-KRAS4A-G12V and 1µg of pCK-hyPBase plasmids were co-electroporated into Im-HUVEC using the P5 Primary Cell Kit (Lonza) and a 4D-nucleofector (Lonza). The program used was CA167. After electroporation, 100µL of FBS was immediately added to the cuvette and incubated at 37°C for 5 minutes. Cells were transferred to a 12-well plate after incubation and grown for 2 days in antibiotic-free media. For antibiotic selection, 0.3mg/mL G418 was added for 5 days with media change every other day. After selection, cells (KRAS4A^{G12V} HUVECs) were expanded and passaged.

2.3 Device Fabrication

AutoCAD was used for creating the device design (supplemental Figure 1A), which was written onto a chrome photomask (Heidelberg upg501 Mask Writer). The standard lithography process supplied by the photoresist manufacturer was used to generate the silicone molds. Briefly, SU-8 2050 photoresist (MicroChem) was spun onto a silicon mold to achieve a 100 µm thick layer. The photomask was used to polymerize (240 mJ/cm^2 exposure energy) the pattern onto the wafer. An optical profiler was used to confirm

bioRxiv preprint doi: https://doi.org/10.1101/2022.01.20.477166; this version posted January 22, 2022. The copyright holder for this preprint (which was not certified by peer review) is the author/funder. All rights reserved. No reuse allowed without permission.

surface and edge finishes of each silicon wafer mold. Silicone mold heights ranged from 90-120 μm.

PDMS was mixed at a 1:10 ratio (elastomer to base) and left to de-gas for 20 min. PDMS was poured onto the wafers inside an acrylic ring so that the final PDMS mold was easily removable. PDMS was baked for 3 hours in the oven at 80°C. After baking, the PDMS was left overnight to cool before removing the PDMS mold. This was to prevent the SU-8 features from peeling off while removing the PDMS. Access holes of 2 mm for the side channels and 1 mm for the tissue chamber were cut out using biopsy punches. PDMS coated glass slides were prepared by spreading 2 mL of PDMS onto a 75 x 50 mm glass slide and baking for 1 hr. Prior to bonding, PDMS molds and PDMS-coated glass slides were covered with packing tape to prevent dust accumulation. The devices were bonded together using plasma treatment (Harrick Plasma). Media reservoirs were created by attaching cryovials that had their bottoms cut out using PDMS (supplemental Figure 1B). The entire device unit was autoclaved before use (supplemental Figure 1C).

2.4 Cell Seeding

24 hours after KRAS4A^{G12V} HUVECs were plated, doxycycline (Sigma-Aldrich) was added in the media (final concentration: 5 μg/mL) to induce KRAS4A^{G12V} expression. Im-HUVECs and NHLF were seeded in fibrin gels (initial concentration: 10 mg/mL bovine fibrinogen) at a 4:1 ratio (Im-HUVECs to NHLF) for a concentration of 10 million total cells/mL. To generate AVM-like microvessels, KRAS^{G12V} Im-HUVECs was combined Im-HUVEC:NHLF cell suspension at the described ratios. The cell suspension was gently pipetted into one side of the tissue chamber until the chamber was filled. Devices were placed in the incubator for 15 min for gel polymerization after which Im-HUVECs were seeded to the side channels coated with 0.1% gelatin for 2 hrs in Vasculife media. During this time, devices were routinely checked and bubbles removed. To establish perfusion, Vasculife media was added in the following volumes to the media reservoir #1: 1500 μL, #2: 1000 μL, #3: 500 μL, #4: 200 μL to achieve an approximate pressure gradient of #1: 23 mm H_2O, #2: 18 mm H_2O #3: 8 mm H_2O, #4: 3 mm H_2O as previously reported [28]. Media reservoirs were refilled every 24 hours. The media flow volume across the tissue

bioRxiv preprint doi: https://doi.org/10.1101/2022.01.20.477166; this version posted January 22, 2022. The copyright holder for this preprint (which was not certified by peer review) is the author/funder. All rights reserved. No reuse allowed without permission.

chamber was reversed (1&3 ↔ 2&4) every 2 days to prevent ECs from migrating to side channels (Figure 1A).

2.5 Microvessel Network Perfusion and Permeability

To assess microvessel perfusion and permeability, 1 mg/mL of 70 kDa dextran conjugated to rhodamine b isothiocyanate (Rhod B, Sigma) was introduced from one media reservoir. Once the dextran solution had perfused the entire vessel network (t=1) images of each diamond within the tissue chamber were acquired at 10 min intervals until 30 min. Images were acquired using the Zeiss AxioObserver Widefield microscope within a 37°C incubation chamber.

2.7 Immunofluorescence Staining

Immunostaining was performed *in situ*, by perfusing all reagents into the device through the side channels. The devices were fixed using 4% paraformaldehyde (PFA) for 20 min at room temperature and washed with PBS overnight. Devices were then permeabilized with 0.05% Tween 20 in PBS and washed for 2-3 hrs with PBS. Then, a blocking solution (5% BSA) was added and incubated overnight at 4°C. VE-cadherin primary antibody (Santa Cruz cat# sc-9989, 1:200 in blocking solution) was incubated overnight at 4°C. Devices were washed with PBS for 4-6 hrs and subsequently incubated with Alexa Fluor 647-conjugated goat anti-mouse IgG (H+L) (ThermoFisher cat# A32728, 1:300) and Hoechst 33342 (Sigma-Aldrich cat# B2261, 1:10000) in blocking solution overnight at 4°C. Devices were washed with PBS and imaged using the Zeiss AxioObserver Widefield microscope.

2.8 Treatment of Microvessel Network

For drug treatment experiments, 25% $KRAS^{G12V}$ vasculatures were treated with 1 µM MEK inhibitor (MEKi, SL327, Sigma) or 10 µM PI3K inhibitor (PI3Ki, LY294002, Sigma) in Vasculife media on days 3 or 5. Treatment was maintained until endpoint (day 7). DMSO was used as a vehicle control.

bioRxiv preprint doi: https://doi.org/10.1101/2022.01.20.477166; this version posted January 22, 2022. The copyright holder for this preprint (which was not certified by peer review) is the author/funder. All rights reserved. No reuse allowed without permission.

2.9 Image Analysis

All images were analysed using Zen blue (ZEISS) and ImageJ (FIJI). All graphs and calculations were done using MATLAB (MathWorks, R2020). Angiotool was used to assess total branch length. Diameter, junction, and branch measurements were done manually using Zen blue. To measure fluorescent intensity in perfusion assays, a binary mask was created from the FITC channel. Two separate images were generated for the intravascular and extravascular perfusion by using the AND operation of the mask and inverse mask over the TRITC channel. The intensity values were then averaged from the intravascular and extravascular images respectively. The permeability coefficient (P) was calculated using the previously described equation [34].

$$P = \frac{D}{4} \times \left(\frac{I_f - I_i}{\Delta t}\right) \times \left(\frac{1}{I_i - I_b}\right)$$

Where D is the average diameter, Δt is the time interval, I_f, I_i, I_b is the fluorescence intensity of the final intravascular, initial intravascular, and background (extravascular) intensity respectively.

2.10 Statistical Analysis

All statistical analyses were preformed with GraphPad Prism 9. All data presented are mean ± standard deviation (SD). One-way ANOVA with Tukey's multiple comparisons test to compare the groups was used to assess significance between 3 groups. The paired two-tailed t-test was used to assess diameter changes over time. The unpaired two-tailed t-test was used to assess significance between 2 groups. A p value <0.05 was considered significant. Each diamond within the tissue chamber was considered a technical replicate (indicated by n), while separate experiments (indicated by N) were considered biological replicates. At least 3 'N' were used for each experimental/seeding condition.

bioRxiv preprint doi: https://doi.org/10.1101/2022.01.20.477166; this version posted January 22, 2022. The copyright holder for this preprint (which was not certified by peer review) is the author/funder. All rights reserved. No reuse allowed without permission.

Results

3.1 Generation of perfused human AVM-like vasculatures *in vitro*

We used a previously described microfluidic device consisting of a central tissue chamber divided into three diamond-shaped chambers, with one port on each end connected to side channels where media is delivered [28,32] (Figure 1A). The 50 µm ports create a single entry and exit in the 1x2 mm diamond chamber and segments the vasculature into three technical replicates (Figure 1A and Supplemental Figure 1A). In this platform, perfusable microvessels were reliably generated *in vitro* over the course of 7 days through self-assembly of endothelial cells (i.e., Im-HUVECs), supported by fibroblasts at a 4:1 ratio. Additionally, the inclusion of endothelial cells in the side channels, generating a monolayer, helped with vessel anastomosis and prevented leakage [32] (Figure 1A). To prevent cells from migrating out of the tissue chamber, the media flow direction was switched between the two side channels every two days by switching inlet function between reservoirs 1&3 to 2&4 (Figure 1A).

For cell seeding (day 0), cells were loaded into the tissue chamber in a fibrin gel. By day 3, ECs extended to neighbouring cells and clustered together to form rudimentary vessels. By day 5, the network structure was clearly established and interconnected. At this time point, microvessels were marginally perfusable (not shown), indicating that the network was lumenized. By day 7, microvessels expanded in diameter to create interconnected, well-perfused, and stable vessel networks (Figure 1B, top panel).

To create the AVM disease model, ECs containing a stably integrated doxycycline-inducible mScarlet (mScar)-KRAS4A^{G12V} expression construct were induced prior to seeding into the microfluidic device [7]. Expression was confirmed by the presence of mScar. KRAS4A^{G12V} ECs were combined with WT-ECs, at 10% or 25% of the total EC number, in fibrin gels and seeded into the microfluidic devices. WT-ECs seeded without KRAS4A^{G12V} ECs acted as controls. Over the course of 7 days, heterogeneous KRAS4A^{G12V} and WT-EC co-cultures effectively self-assembled into perfusable microvessels (Figure 1B, middle and bottom panels). In devices containing KRAS4A^{G12V} ECs, mScar-positive segments were present within the vessel network, confirming that the KRAS4A^{G12V} ECs had integrated into the vasculature (Figure 1B, C). As expected,

bioRxiv preprint doi: https://doi.org/10.1101/2022.01.20.477166; this version posted January 22, 2022. The copyright holder for this preprint (which was not certified by peer review) is the author/funder. All rights reserved. No reuse allowed without permission.

vasculatures with KRAS4A^{G12V} ECs had distinct aberrant vessel structures. Vascular networks containing 25% KRAS4A^{G12V} ECs resembled vascular plexuses rather than the typical microvascular networks formed using WT-ECs (Figure 1B, C).

To assess potential changes in vessel diameter associated with mutant KRAS expression, the width of individual microvessels in the 25% KRAS vasculatures were measured on day 7. Vessel width in the 25% KRAS microvessels was larger and highly heterogenous compared to 0% KRAS, resulting in a larger distribution (Figure 1D). In line with human brain AVMs, we found that vessel segments in 25% KRAS microvessels with KRAS4A^{G12V} ECs were significantly wider than vessel segments within the same network that lacked KRAS4A^{G12V} ECs, measuring 47.3 ± 28.5 μm and 18.2 ± 7.2 μm, respectively (Figure 1E). There was no significant difference between vessel widths in mixed cultures in sections without KRAS and the vessel width in wild-type monocultures (i.e., 0% KRAS) (17.5 ± 7.3 μm) (Figure 1E). This demonstrated that vessel enlargement only occurs where KRAS4A^{G12V} ECs are present, but this does not affect surrounding vessels formed by WT-ECs within the same network. Unfortunately, it was not possible to assess vessel width of KRAS4A^{G12V} EC vessels in the 10% KRAS networks, as KRAS4A^{G12V} ECs mainly concentrated in vessel junctions when seeded at low ratios (Figure 1C, center image). Hereafter, vasculatures generated with 0%, 10%, and 25% KRAS4A^{G12V} ECs at seeding will be referred to as 0%, 10% and 25% KRAS vasculatures respectively.

3.2 Changes in vessel network parameters towards AVM-like morphology

To assess the morphological and functional changes in vessel networks formed with KRAS4A^{G12V} ECs, we evaluated branch length, junction number, and vessel area coverage. As a result of vessel enlargement, the total area covered by the vessel network is greater in 10% and 25% KRAS microvessels (50.0 ± 3.2% and 53.4 ± 3.5%, respectively), and significantly higher than 0% KRAS microvessels (42.1 ± 6.9%) (Figure 2A).

We next visualized where the mutant KRAS cells localize in the network. In 10% KRAS vasculatures, KRAS4A^{G12V} ECs preferentially localized in vessel junctions at a significantly higher rate than expected if this was a random process, and were depleted at branches, as shown in Fig. 1C and quantified in Fig. 2B. Seventy eight ±9.0% of

bioRxiv preprint doi: https://doi.org/10.1101/2022.01.20.477166; this version posted January 22, 2022. The copyright holder for this preprint (which was not certified by peer review) is the author/funder. All rights reserved. No reuse allowed without permission.

KRAS4A^{G12V} ECs localized at junctions compared to 22.0±9.0% localizing at vessel branch segments. Despite the increased frequency of KRAS-ECs at the junctions, the number of junctions in each vasculature was not significantly different (Figure 2C). Conversely, there was a significant increase in the number of branches between 0% KRAS (67.5±9.7) and 25% KRAS (90.0±24.2) vasculatures (Figure 2D), indicating that there were more branches extending from a single junction.

The average branch length in the overall network decreased from 190.1±70.0 μm in 0% KRAS to 160.7±58.3 μm in 10% KRAS and 101.8±20.1 μm in 25% KRAS vasculatures (Figure 2E). As a result of the inverse relationship between average branch length and count, the total branch length, being the length of all the vessel segments end-to-end, was not significantly different. The total branch length was 9.4±2.3, 7.2±2.0, and 7.8±1.1 mm in the 0%, 10%, and 25% KRAS microvessels, respectively (Figure 2F). Taken together, these measurements indicate that the inclusion of KRAS4A^{G12V} ECs in microvessel formation affected the overall vessel networks by shortening branch length and increasing vessel density.

By counting the number of cells in vessel segments with only GFP or mScar cells, we determined that the average cell density in vessels made from WT-ECs was two times higher than that of mScar KRAS4A^{G12V}-ECs (1.7 and 0.8 cells/1000 μm^2, respectively). This suggests that the resulting enlargement of microvessels in 10% and 25% vasculatures is not the result of an excessive number of ECs and that instead it is due to an increase in the size of KRAS4A^{G12V} ECs (Figure 2G).

3.3 AVM-like vessels display increased permeability

To test whether KRAS microvessels exhibited weakened barrier integrity, we assessed the extravasation of 70 kDa dextran conjugated to rhodamine b isothiocyanate (rhod B). On day 7, dextran-rhod B was added to the inlet and allowed to perfuse throughout the vasculature (denoted as time = 1 min). Time course images taken every 10 mins up to 30 mins after initial dextran perfusion confirmed that the control microvessel network was intact and lumenized, showing physiological barrier properties. Additionally, this also demonstrated that vessels were well connected to the inlets and outlets of the tissue chamber. No focal leakage was observed (Figure 3A, top panel). Conversely, we

bioRxiv preprint doi: https://doi.org/10.1101/2022.01.20.477166; this version posted January 22, 2022. The copyright holder for this preprint (which was not certified by peer review) is the author/funder. All rights reserved. No reuse allowed without permission.

observed an increase in interstitial fluorescence intensity over time in both 10% and 25% KRAS vasculatures, demonstrating increased permeability (Figure 3A, middle and bottom panel). In 10% KRAS microvessels, rhod B dextran was observed leaking from a singular point, originating from the vessel junction in 15% of the devices (Figure 3A, middle panel). In the other 10% KRAS vasculatures there was no apparent source of leakage. Instead, an overall increase in interstitial fluorescence intensity was observed. In the 25% KRAS microvessels, the overall vasculature was more permeable to rhod B dextran and there was progressive leakage throughout the chamber due to the widespread distribution of KRAS4A^{G12V} ECs throughout the vascular network (Figure 3A, bottom panel). No focal points of vessel leakage were observed. Quantification of the fluorescence intensity demonstrated there was a significant increase in extravascular Dextran-rhod B in 25% KRAS microvessels compared to 0% KRAS microvessels (45.1±22.7 and 49.6±22.2 respectively, Figure 3B), as assessed by measuring the fluorescence intensity in the lumen and extravascular space and normalizing to the interstitial lumen intensity at 1 min. This value is displayed as a ratio of extravascular over intravascular intensity. The permeability coefficient was also calculated and indicated that there was a significant increase in vessel permeability in 10% and 25% KRAS vasculatures (14.3±8.1 and 22.7±7.6 x10^{-2} μm/s) compared to 0% KRAS vasculature (2.46±1.1 x10^{-2} μm/s) (Figure 3C). The observed increased vessel permeability in 10% and 25% KRAS vasculatures is consistent with poor vascular integrity in human AVMs.

To investigate a potential cause of barrier dysfunction, we stained for the cell-cell adhesion molecule VE-cadherin, previously implicated in KRAS4A^{G12V} EC permeability defects in monolayers [5,7]. Indeed, immunofluorescence staining showed that there was a reduction in VE-cadherin staining at the cell junctions of KRAS4A^{G12V} ECs (Figure 3D, arrows). The junctions of surrounding WT-ECs remained intact and unaffected. This confirmed that the increased permeability of the KRAS microvessel network is due to the disruption of adherens junctions in the KRAS4A^{G12V} ECs, thus, recapitulating the compromised barrier function associated with AVMs.

3.4 Improvement of vessel barrier function by treatment with a MEK Inhibitor

bioRxiv preprint doi: https://doi.org/10.1101/2022.01.20.477166; this version posted January 22, 2022. The copyright holder for this preprint (which was not certified by peer review) is the author/funder. All rights reserved. No reuse allowed without permission.

An important goal of a human model of AVM *in vitro* is to assess the effects of potential drugs in both structural and functional hallmarks of AVMs in a human-relevant model. We treated established 25% KRAS vasculatures with a MEK inhibitor (MEKi, SL327 [5,7]) and assessed vessel permeability. DMSO and a PI3K inhibitor (PI3Ki, LY294002) acted as controls. PI3K is a downstream effector of KRAS in other cell types, but is not activated in KRAS4A^{G12V} ECs [5]. To understand if MEKi would reverse established AVM defects, drug treatments started on day 5 (Figure 4A) when vessel networks were stable. Vessel permeability to 70 KDa MW dextran-rhod B was assessed on day 7 post-seeding.

Image analysis showed that treatment with MEKi led to a robust reduction in interstitial fluorescence intensity of the 25% KRAS vasculatures (Figure 4B, middle panel) compared to DMSO- or PI3Ki-treated vasculatures (Figure 4B, top and bottom panels, respectively). In the MEKi-treated microvessels, there was no apparent leakage. Assessment of the normalized fluorescent intensity ratio showed a significantly lower permeability in MEKi-treated vasculature (Figure 4C, 12.5±5.8) compared the DMSO and PI3Ki (Figure 4C, 44.3±12.7 and 55.2±7.5, respectively). As expected, assessment of the permeability coefficient corroborates findings from the analysis of fluorescent intensity, with the MEKi-treated networks displaying significantly lower permeability (9.0±7.0 x10^{-2} µm/s) than DMSO- or PI3Ki-treated networks (23.1±9.5 x10^{-2} and 21.6±6.4 x10^{-2} µm/s, respectively) (Figure 4D). Immunofluorescent staining of MEKi treated vasculatures showed partial restoration of cell-cell junction localization of VE-cadherin in KRAS4A^{G12V} ECs, suggesting a role for cell-cell VE-cadherin binding in the reduction of vessel permeability. In the DMSO and PI3K treated microvessels, KRAS4A^{G12V} ECs still lacked VE-cadherin, while WT-ECs cell junctions remained intact (Figure 4E).

Next, we questioned if the restoration of barrier in AVM-like vasculatures by the MEKi would be accompanied by a concomitant decrease in vessel width. Vessel width was highly heterogeneous and there were no changes in width in response to drug treatment (Figure 5A). The average vessel width was 45.1±22.7, 46.8±18.5, 49.6±22.2 µm for the DMSO, MEKi, and PI3Ki treatments, respectively (Figure 5B), which indicates that treatment with MEKi for 2 days is not effective in reversing vessel enlargement.

We then tested if treatment with MEKi at an earlier time point, when the vasculature was not yet fully formed, would prevent KRAS4A^{G12V} EC-induced vessel enlargement.

bioRxiv preprint doi: https://doi.org/10.1101/2022.01.20.477166; this version posted January 22, 2022. The copyright holder for this preprint (which was not certified by peer review) is the author/funder. All rights reserved. No reuse allowed without permission.

Therefore, we started drug treatment at day 3 post-seeding and assessed vessel width at day 7. Interestingly, treatment with the MEKi starting at day 3 did not prevent vessel enlargement (Figure 5C, D) indicating that EC assembly into microvessels was not affected by MEKi treatment (Figure 5D). In addition, a comparison of vessel widths between 25% KRAS vasculatures treated with MEKi beginning on day 3 or 5 showed that treatment with MEKi did not affect vessel width distribution (Figure 5E) and that the average vessel width at the endpoint (Day 7) was the same (Figure 5F).

bioRxiv preprint doi: https://doi.org/10.1101/2022.01.20.477166; this version posted January 22, 2022. The copyright holder for this preprint (which was not certified by peer review) is the author/funder. All rights reserved. No reuse allowed without permission.

Discussion

The events that take place during AVM initiation and development are still not well understood. As a result, there is a lack of pharmacological treatment options. In this study, we combined WT ECs with ECs harbouring the KRAS4A^{G12V} mutation and generated the first *in vitro* microfluidic model of AVMs. This heterogeneous mixture of mutant and normal ECs was chosen to reflect the heterogeneity found in clinical samples of AVMs [5]. This platform focuses on the specific KRAS4A^{G12V} contributions to the early steps in vessel formation. The resulting microvessel network recapitulates the key hallmarks of AVM: vessel dilation and increased permeability. Apart from vessel enlargement, the AVM-like microvessels were particularly noted for their irregular shape. Previous studies of KRAS4A^{G12V} EC cultures reported changes to EC phenotype, which included increased cell size and irregular cell shape [5]. Within the 3D tubular vessel structure, we also observed that KRAS4A^{G12V} ECs displayed increased cell size compared to the vessels formed by WT-ECs in the same microvessel network. In addition, we demonstrated that vessel enlargement was cell-autonomous in cells expressing KRAS4A^{G12V} and did not affect surrounding vessels in the same network without the KRAS4A^{G12V} mutation. Additionally, defective VE-cadherin localization was observed only in KRAS4A^{G12V} ECs and not in WT-ECs. Thus, the KRAS4A^{G12V} ECs are necessary and sufficient for eliciting the disease phenotype. The resulting enlarged vessels also led to an increased vessel area coverage, with significantly shorter vessel branches and an increased ratio of branches to junctions. Additionally, KRAS4A^{G12V} ECs localized preferentially to vessel junctions, resulting in vessel junctions that were much more prominent.

Previously, KRAS4A^{G12V} ECs have also been noted in monolayers[5] for their abnormally large shape. Here we speculate that the same KRAS4A^{G12V} ECs morphology within the microvessel network responsible for vessel enlargement. Our evidence in a human-relevant model indicates that enlarged vessel lumens are a consequence of the increased EC size and not EC proliferation. Further investigation will be done to determine if these enlarged lumens of KRAS-mutant vessels will result in increased shear stress leading to abnormal cellular mechanosensory responses or create turbulent shear to disrupt vascular homeostasis [35].

bioRxiv preprint doi: https://doi.org/10.1101/2022.01.20.477166; this version posted January 22, 2022. The copyright holder for this preprint (which was not certified by peer review) is the author/funder. All rights reserved. No reuse allowed without permission.

One limitation to note is that when measuring the branch length in the KRAS4A^{G12V} conditions, all vessels in the network were included. Some vessels may not have been KRAS4A^{G12V} positive. In addition, most vessels were likely not parallel to the XY plane so the length measured would only be the components in the XY direction. As a result, this would influence the vessel width and length measurements. Given the 100 µm height of the chamber in relation to the average vessel width that ranged from 20-60 µm, we assumed that the Z component length would be very small and negligible.

Another key feature of the AVM-on-a-chip model is that it recapitulated increased permeability at the site of KRAS4A^{G12V} positive vessel segments due to the loss of VE-cadherin^{+} adherens junctions. Similarly to the diameter measurements, the KRAS4A^{G12V} ECs do not influence surrounding WT-EC to adopt the same intercellular junction disruption. Previous transwell leakage assays showed increase permeability due to breakdown of VE-cadherin junctions[7]. Here, we have showed that increased permeability is also a feature of AVM-like microvessels generated from KRAS4A^{G12V} ECs, despite the presence of luminal flow which is a known cue for vessel barrier tightening [36,37].

These findings are also consistent with findings in the KRAS4A^{G12V} zebrafish model [7]. However, *Nikolev et al*.[5] demonstrated that KRAS mutations made up only a small fraction of AVM tissue samples where vessel enlargement or nidus formation was present throughout the sample rather than only localizing to mutant EC segments. Given that clinical AVMs take several years to progress it is likely that the AVM-like vasculatures formed here capture only the onset of nascent AVM that have yet to remodel into the complex nidus that includes wild-type and KRAS mutant cells. An alternative explanation could be that a “second hit” (e.g. from an environmental factor) is necessary to induce more severe presentations of the disease that is typically diagnosed in patients [38]. In the future, we can use this platform to investigate potential effects of increased flow rates/shear stress in AVM-like vessels. It is well known that disturbed flow, typically developed in junctions and curvature, results in EC dysfunction in vascular disease [39]. Considering the enlarged junctions, where KRAS4A^{G12V} HUVECs preferentially reside, and irregularly shaped branches, these areas would be susceptible to creating disturbed flow and potentially a maladaptive mechanosensory response.

bioRxiv preprint doi: https://doi.org/10.1101/2022.01.20.477166; this version posted January 22, 2022. The copyright holder for this preprint (which was not certified by peer review) is the author/funder. All rights reserved. No reuse allowed without permission.

Some studies have suggested that AVM formation is an inappropriate angiogenic response characterized by defective vessel maturation [8,12,40,41]. Indeed, brain AVMs have been previously shown to harbor increased expression of angiogenic genes and downstream VEGF signalling [42–44]. KRAS^{G12V} ECs were also found to have elevated levels of VEGF and a transcriptional signature that resembles VEGF stimulated cells [5]. This may explain the breakdown of VE-cadherin junctions that we have observed in the AVM-like microvessels, typically associated with early angiogenic stages [45–47]. Although no overt signs of angiogenesis were seen in the AVM-like vessels (e.g. sprouting), the increase in branch number is suggestive of increased vessel formation in KRAS4A^{G12V} vasculatures.

In previous monoculture and animal models, MEKi has been investigated as a possible treatment strategy [5,7,22,48,49]. In monocultures, MEKi re-established VE-cadherin to cell junctions and restored normal actin localization and cell shape by suppressing ERK phosphorylation [5]. Transwell assays of KRAS4A^{G12V} HUVECs showed reduced permeability with treatment of MEKi after 18 hours. In zebrafish models, MEKi was effective in reversing vessel enlargement and hemorrhagic events [7]. Mouse models of brain AVMs resulting from delivery of brain trophic AAV-KRAS^{G12V} revealed that treatment before AVM development led to significantly less brain AVMs and improved cognitive function [22]. We have demonstrated that treatment with MEKi recovered VE-cadherin localization in KRAS4A^{G12V} HUVECs, which resulted in improved vascular wall integrity. However, treatment with MEKi did not reverse (i.e., treatment at day 5 post-seeding when microvessels are mostly formed and there is perfusion) or prevent (i.e., treatment at day 3 post-seeding prior to the formation of an interconnected vessel network) vessel enlargement. With this platform, we were able to uncouple vessel enlargement and improved vascular permeability and showed that these two hallmarks and their presences are not completely dependent on each other, which was previously not demonstrated.

Based on difference in microvessel formation, there is an innate difference at the cellular level of the KRAS4A^{G12V} HUVECs that may act independently from the MAPK/ERK pathway. Perhaps, there are other contributing pathways that require exogenous initiation [38]. With this platform, we can systematically assess and isolate external factors such as inflammation, increased fluid flow, and tissue-specific interactions.

bioRxiv preprint doi: https://doi.org/10.1101/2022.01.20.477166; this version posted January 22, 2022. The copyright holder for this preprint (which was not certified by peer review) is the author/funder. All rights reserved. No reuse allowed without permission.

The inability of a MEKi to reduce vessel size in AVM-like vessels suggests that KRAS signaling may be affecting another pathways/protein apart from downstream MEK, leading to an increase in cell size. KRAS has been implicated as one of the common drivers for cancer and plays a central role in several cellular signalling pathways [5,6,50,51]. As a result, targeting the MAPK/ERK and KRAS protein activity for cancer treatment is of high interest. Most recently, case reports detailing the use of the MEKi Trametinib has improved AVMs, including an overall reduction in patient AVM size [52,53]. We speculate that reduced pericyte coverage and paracrine signalling may play a role in AVM vessel stability [54]. In 3D collagen co-cultures of KRAS4A^{G12V} HUVECs and pericytes, the KRAS4A^{G12V} HUVECs formed abnormally wide tubes with a lack of pericyte recruitment compared to normal HUVECs. Additionally, there was a decrease of basement membrane protein deposition, suggesting a lack of pericyte-induced maturation [55]. In the future, pericytes can be included in the microfluidic devices to better mimic vessel composition [29,30,56]. In doing so, we can gain new insight into KRAS4A^{G12V} EC crosstalk with pericytes and whether the lack of pericyte association exacerbates the AVM phenotype [14]. In the present form, the AVM-on-a-chip model described here has focused on the contribution of the KRAS4A^{G12V} mutation to AVM formation/initiation. We demonstrated that the mutation is responsible for increased cell size and loss of VE-cadherin.

In conclusion, we have developed and validated an AVM-on-a-chip platform using a mosaic composition of WT-ECs and KRAS4A^{G12V} ECs that is sufficient to drive AVM defects: vessel distension and hyperpermeability. These findings confirm previous results in 2D monolayer culture and animal models and provide new insight into the 3D mechanism of the KRAS4A^{G12V} mutation [5,7]. Additionally, this platform represents an ideal method to create other vascular disease models *in vitro* using mutant EC cell lines. We know that several vascular malformations (venous, capillary, cavernous, telangiectasis, and arteriovenous malformation) have been associated with genetic mutations [57,58]. The hereditary form of AVMs, HHT has been linked to mutations in *SMAD4*, *ALK1*, and *ENG* [3,7,42,43]. Additionally, there have been other mutations identified in the MAP2K1 pathway (*HRAS*, *BRAF*, and *MAP2K1*) associated with AVM [4,61]. Cerebral cavernous malformations (CCMs) are caused by several different mutations in *KRIT1*, *CCM1,23*, or

bioRxiv preprint doi: https://doi.org/10.1101/2022.01.20.477166; this version posted January 22, 2022. The copyright holder for this preprint (which was not certified by peer review) is the author/funder. All rights reserved. No reuse allowed without permission.

PDCD10 gene [62]. It is currently unclear how mutations in these disparate genes alter EC phenotype to drive vascular malformations. This platform would be of interest to gain a better understanding of the disease phenotypes resulting from these EC mutations. In this way, gene-specific differences in AVM formation and other vascular malformations may be revealed. Importantly, the platform described here can be used to test pharmacologic treatments for these vascular malformations.

bioRxiv preprint doi: https://doi.org/10.1101/2022.01.20.477166; this version posted January 22, 2022. The copyright holder for this preprint (which was not certified by peer review) is the author/funder. All rights reserved. No reuse allowed without permission.

Acknowledgements

This work was supported by grants from the Canadian Institutes of Health Research (CIHR) (CIHR PJT153160) and a Discovery grant from the Natural Sciences and Engineering Research Council (NSERC RGPIN 06621-2017) to S.S.N and grants from CIHR (CIHR PJT155922) and the U.S. Department of Defense (W81XWH-18-1-0351) to Dr. J. Wythe and J.E.F. K.S. was partially supported from the Mount Sinai Hospital Graduate Scholarship in Science and Technology. M.L. was partially supported from the NSERC CREATE Training program in organ-on-a-chip engineering and entrepreneurship (TOeP) and Wildcat Graduate Scholarship. R.W. was supported by a Canada Graduate Scholarship from CIHR. We thank Dr. R. Kamm for providing the IM-HUVECs (GFP WT-ECs), Dr. J. Wythe provided the hTERT-HUVEC and plasmid used to create the mutant KRAS EC line, O. Mourad for the support with statistical analysis. K.S. conducted majority of the experiments and wrote the manuscript. M.L. contributed to image analysis and experimental repeats. R.W. developed and validated the $KRAS^{G12V}$ inducible IM-HUVEC line and designed the MEKi experiment. Dr. J. Wythe designed and tested the $KRAS^{G12V}$ inducible constructs. J.E.F. provided supervision to R.W., designed experiments and revised the manuscript. S.S.N. provided supervision and guidance for this project and contributed to manuscript writing and revisions.

bioRxiv preprint doi: https://doi.org/10.1101/2022.01.20.477166; this version posted January 22, 2022. The copyright holder for this preprint (which was not certified by peer review) is the author/funder. All rights reserved. No reuse allowed without permission.

Manuscript Figure Legends

Figure 1: Generation of a perfused human AVM-like vasculature-on-a-chip (A) Schematic representation of the experiments and timelines. (B) Representative time course of vessel network formation using different ratios of wild-type (WT)- and KRAS4A^{G12V}-ECs. Images of cell suspension immediately after seeding on day 0. WT-ECs (green) and KRAS4A^{G12V} ECs (red) are round and evenly distributed within the fibrin gel. By day 3, tube-like structures begin to form as they migrate towards each other. By day 5, microvessel connections and network shape begins to stabilize. By day 7, the microvessel network is fully interconnected, lumenized and perfused. (Scale bar 500 μm). (C) Zoomed fluorescent images of microvessel segments of 0% KRAS4A^{G12V} (control), 10% KRAS4A^{G12V}, 25% KRAS4A^{G12V} vasculatures (scale bar, 50 μm) (D) Distribution of microvessel width measurements in 25% KRAS4A^{G12V} vasculatures between segments without KRAS4A^{G12V} ECs (green) and segments with some visible KRAS4A^{G12V} (red) (bin size: 10 μm). KRAS4A^{G12V} positive vessel distribution is much wider and variable compared to vessel with no KRAS4A^{G12V} (E) Quantification of the average diameter in microvessel networks in 0% KRAS4A^{G12V} ECs (blue) compared to 25% KRAS4A^{G12V} microvasculatures with (red) and without (green) KRAS4A^{G12V} ECs. (One-way ANOVA with Tukey's multiple comparison test; ***$p < 0.001$, N=3; mean ± SD)

Figure 2: Quantification of AVM-like microvessel morphological characteristics. Quantification of (A) area coverage of 0% (blue), 10% (yellow), and 25% KRAS4A^{G12V} (red) microvasculatures. (One-way ANOVA with Tukey's multiple comparison test; **$p < 0.01$, ***$p < 0.001$, N=3; mean ± SD) (B) Incidence rate of KRAS4A^{G12V} located in vessel junctions (left) compared to branches (right) in 10% KRAS4A^{G12V} microvasculatures. (Unpaired Student's t-test; ***$p < 0.001$, N=3; mean ± SD). Quantification of (C) number of junctions, (D) number of branches, (E) average branch length, and (F) total branch length of 0% (blue), 10% (yellow), and 25% KRAS4A^{G12V} (red) microvasculatures. (One-way ANOVA with Tukey's multiple comparison test; *$p < 0.05$, **$p < 0.01$, N=3; mean ± SD) (G) The number of cells counted in GFP^{+} (green) or mScarlet^{+} (red) vessel segments normalized to 1000 um^2 vessel area. (Unpaired Student's t-test; ***$p < 0.001$, N=3; mean ± SD)

bioRxiv preprint doi: https://doi.org/10.1101/2022.01.20.477166; this version posted January 22, 2022. The copyright holder for this preprint (which was not certified by peer review) is the author/funder. All rights reserved. No reuse allowed without permission.

Figure 3: AVM-like microvessels display increased permeability. (A) Representative time course images of microvessel perfusion with 70 kDa dextran conjugated to rhodamine-B (rhod B). The 1 min timepoint denotes the moment vessels are initially fully perfused with dextran. White arrows in middle panel show leakage originating from vessel (scale bar 500 μm). (B) Quantification of microvessel 70 kDa dextran-rhod B intensity normalized to t=1 of 0% (blue), 10% (yellow), and 25% (red) KRAS4A^{G12V} microvasculatures. Fluorescence intensity was measured as a ratio of interstitial to lumen intensity then normalized to t=1. 25% KRAS4A^{G12V} microvasculatures showed a significant increase in interstitial intensity after 30 min. (C) Permeability coefficient of 0% (blue) 10% (yellow) and 25% (red) KRAS4A^{G12V} microvessel conditions. There was a significant increase in permeability as the percentage of KRAS4A^{G12V} increased. (One-way ANOVA with Tukey's multiple comparison test; N=3, *$p < 0.05$, ***$p < 0.001$; mean ± SD) (D) Immunofluorescence images of 0% and 25% KRAS4A^{G12V} EC microvasculatures on day 7. VE Cadherin (purple) staining is reduced in areas (indicated by arrow) with KRAS4A^{G12V} EC (white) but remains intact throughout the rest of the vessel network with normal ECs (green). (scale bar 100 μm).

Figure 4: MEK inhibition restores vessel integrity of AVM-on-a-chip. (A) Schematic of drug treatment protocol. (B) Time course images of microvessel perfusion with 70 kDa dextran-rhod B (scale bar 500 μm). (C) Quantification of microvessel 70 kDa dextran-rhod B intensity normalized to t=1 of 25% KRAS4A^{G12V} microvasculatures treated with different drugs starting at day 5. Fluorescent intensity was measured as a ratio of interstitial to lumen intensity normalized to t=1. MEKi-treated AVM-like microvasculatures displayed significantly lower dextran extravasation than DMSO or PI3Ki. (D) Permeability coefficient of 25% KRAS4A^{G12V} microvasculatures treated with DMSO (gray), MEKi (orange) or PI3Ki (purple). The permeability of MEKi treatment microvasculatures was significantly lower than that of DMSO or PI3Ki treated AVM-like vessels. (One-way ANOVA with Tukey's multiple comparison test; N=3, ***$p < 0.001$; mean ± SD) (E) Immunofluorescence images of day 5 treated AVM-on-a-chip. MEKi-treated AVM-like microvasculatures have an increase in VE-cadherin (purple) rich adherens junction staining in KRAS4A^{G12V} ECs (white, arrows indicate areas of increased VE-cadherin)

bioRxiv preprint doi: https://doi.org/10.1101/2022.01.20.477166; this version posted January 22, 2022. The copyright holder for this preprint (which was not certified by peer review) is the author/funder. All rights reserved. No reuse allowed without permission.

compared to DMSO or PI3Ki treatment (arrows indicate areas of VE-cadherin disconnect) (scale bar 100 μm).

Figure 5: MEK inhibition does not affect width of AVM-on-a-chip (A) Day 7 distribution of 25% KRAS4A^{G12V} microvessel widths treated with different drugs starting at day 5. (bin size: 10 μm). (B) Average vessel width at day 7 of 25% KRAS4A^{G12V} microvessel treated with DMSO, MEKi, or PI3Ki starting at day 5 show no significant differences. (One-way ANOVA with Tukey's multiple comparison test; N=3; mean ± SD). (C) Day 7 images of KRAS4A^{G12V} microvessels treated with MEKi starting at day 3 (scale bar 500 μm). (D) Average vessel width of 25% KRAS4A^{G12V} microvasculatures before (day 3) and after (day 7) treatment with MEKi starting day 3. (Paired Student's t-test; N=3; mean ± SD). (E) Day 7 vessel width distribution of 25% KRAS4A^{G12V} microvasculaturs treated with MEKi starting on day 3 or day 5. (bin size: 10 μm). (F) Average day 7 vessel width of 25% KRAS4A^{G12V} microvasculatures treated with MEKi starting on day 3 or day 5. (Unpaired Student's t-test; N=3; mean ± SD).

bioRxiv preprint doi: https://doi.org/10.1101/2022.01.20.477166; this version posted January 22, 2022. The copyright holder for this preprint (which was not certified by peer review) is the author/funder. All rights reserved. No reuse allowed without permission.

Manuscript Supplemental Figures Legends

Supplemental Figure 1. Fabrication of Devices (A) Design of microfluidic device. Three overlapping diamond channels (tissue chamber, red) are connected to two parallel 100 µm wide side channels through a 50 µm long port. Side channels are used to perfuse media into the tissue chamber during microvessel formation. The length of media channels and gel loading channel were arbitrarily chosen for ease of handling. (B) Schematic of fabrication process. PDMS negative molds were made from silicon wafers with design etched on. 2 µm inlets were punched for the media ports and 1 µm used for gel loading. The PDMS mold was plasma bonded onto glass slide coated with PDMS. Cryovials were glued on using PDMS, acting as media reservoirs. (C) Photo of assembled microfluidic device.

Supplemental Figure 2. Luminal and interstitial intensity of AVM-like microvessels. Raw intensity values of vessel lumen (black) and interstitial space (red) measured at 1, 10, 20 and 30 minutes following injection of 70 kDa rhod B dextran of (A) 0%, (B) 10%, and (C) 25% KRAS4A^{G12V} microvasculatures. (N=3)

bioRxiv preprint doi: https://doi.org/10.1101/2022.01.20.477166; this version posted January 22, 2022. The copyright holder for this preprint (which was not certified by peer review) is the author/funder. All rights reserved. No reuse allowed without permission.

Manuscript Figures

Figure 1

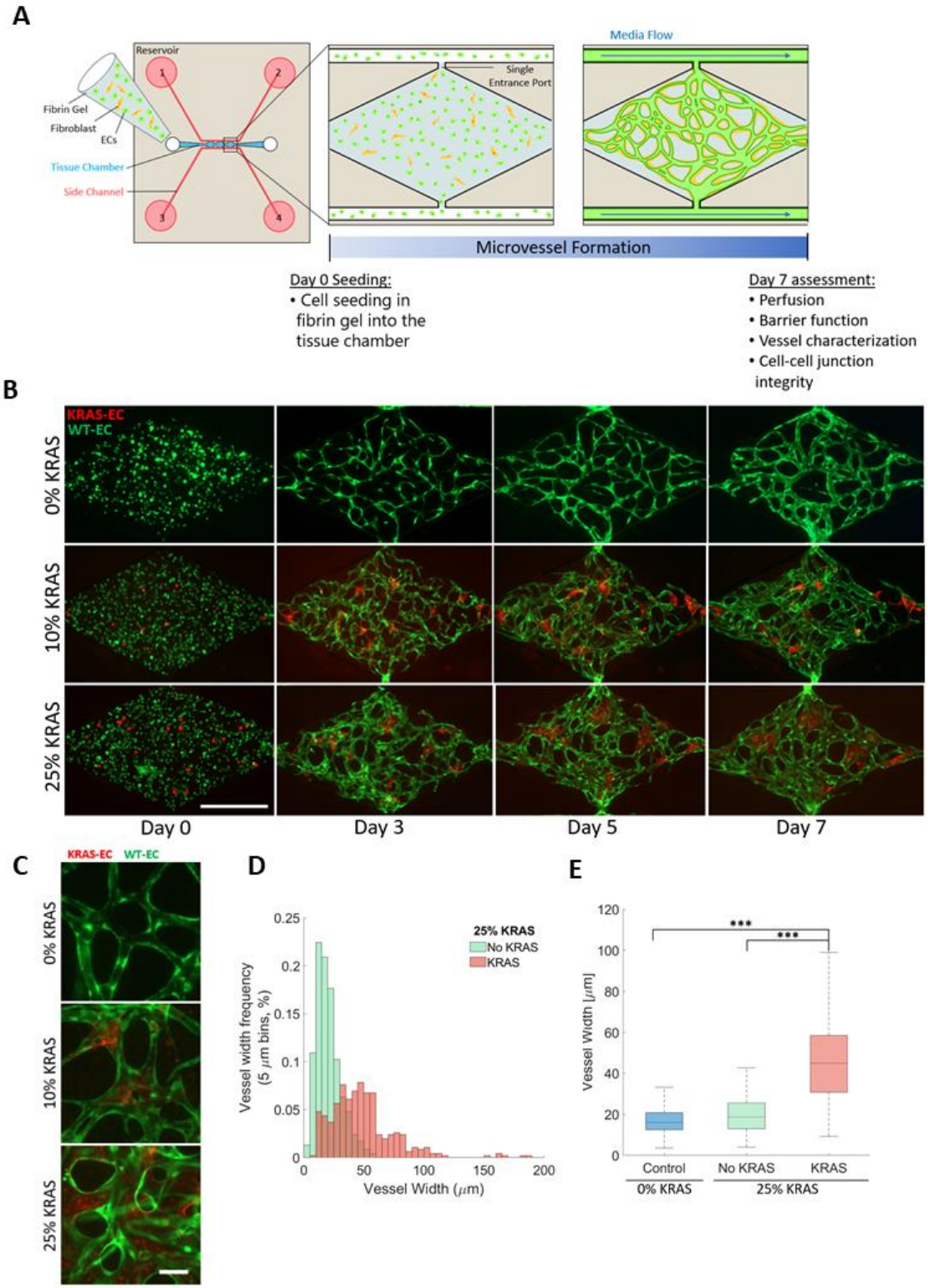

bioRxiv preprint doi: https://doi.org/10.1101/2022.01.20.477166; this version posted January 22, 2022. The copyright holder for this preprint (which was not certified by peer review) is the author/funder. All rights reserved. No reuse allowed without permission.

Figure 2

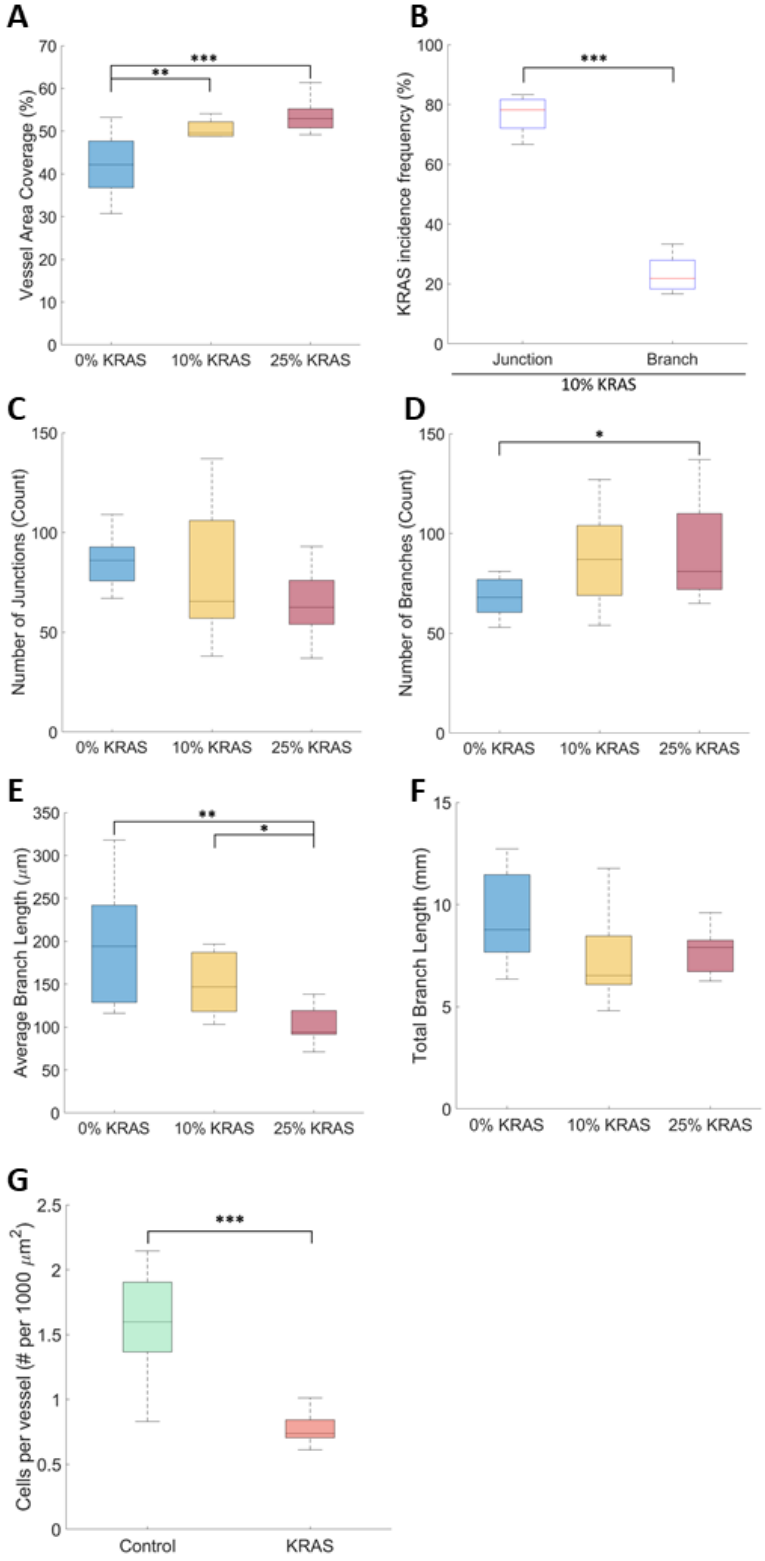

bioRxiv preprint doi: https://doi.org/10.1101/2022.01.20.477166; this version posted January 22, 2022. The copyright holder for this preprint (which was not certified by peer review) is the author/funder. All rights reserved. No reuse allowed without permission.

Figure 3

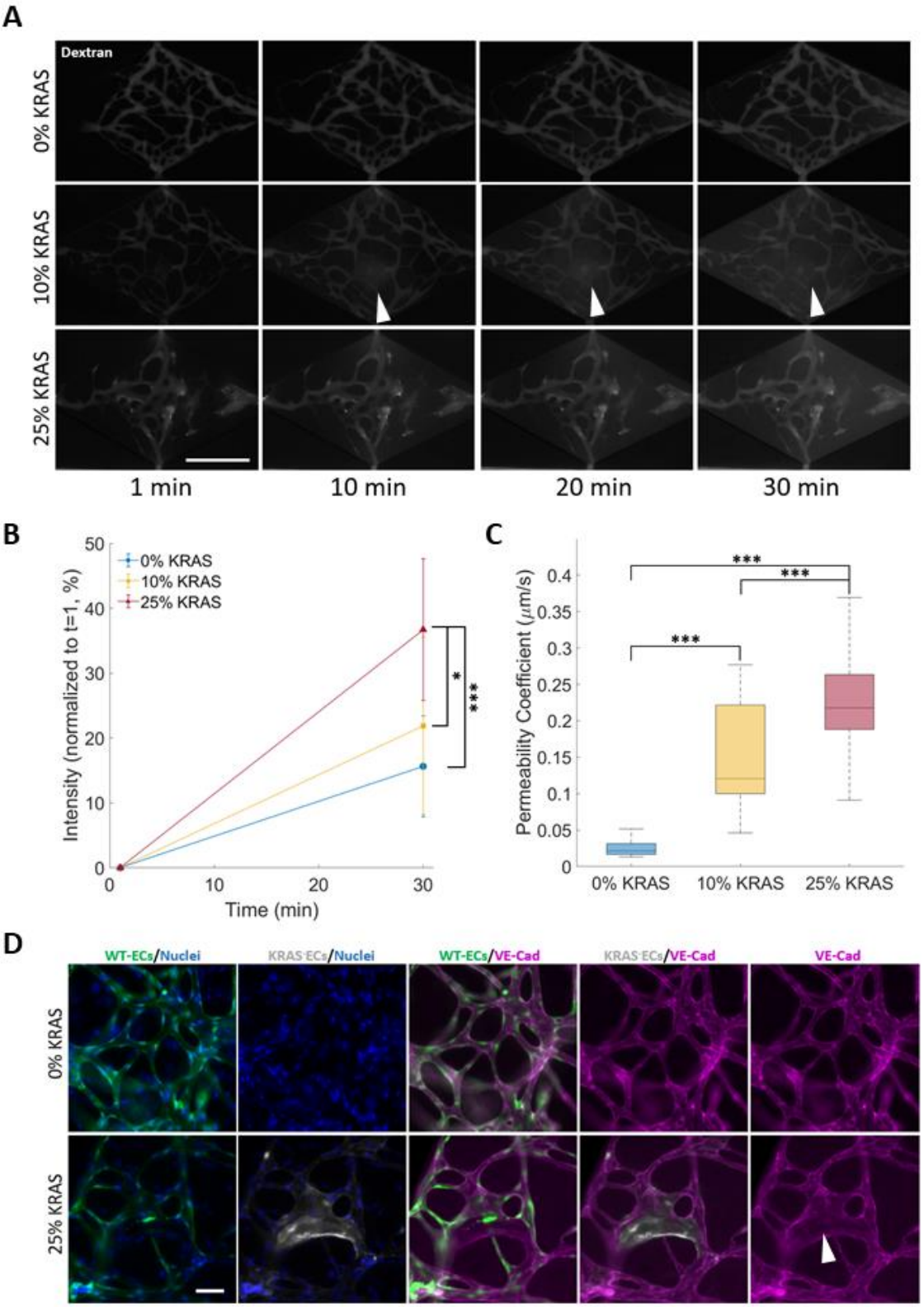

bioRxiv preprint doi: https://doi.org/10.1101/2022.01.20.477166; this version posted January 22, 2022. The copyright holder for this preprint (which was not certified by peer review) is the author/funder. All rights reserved. No reuse allowed without permission.

Figure 4

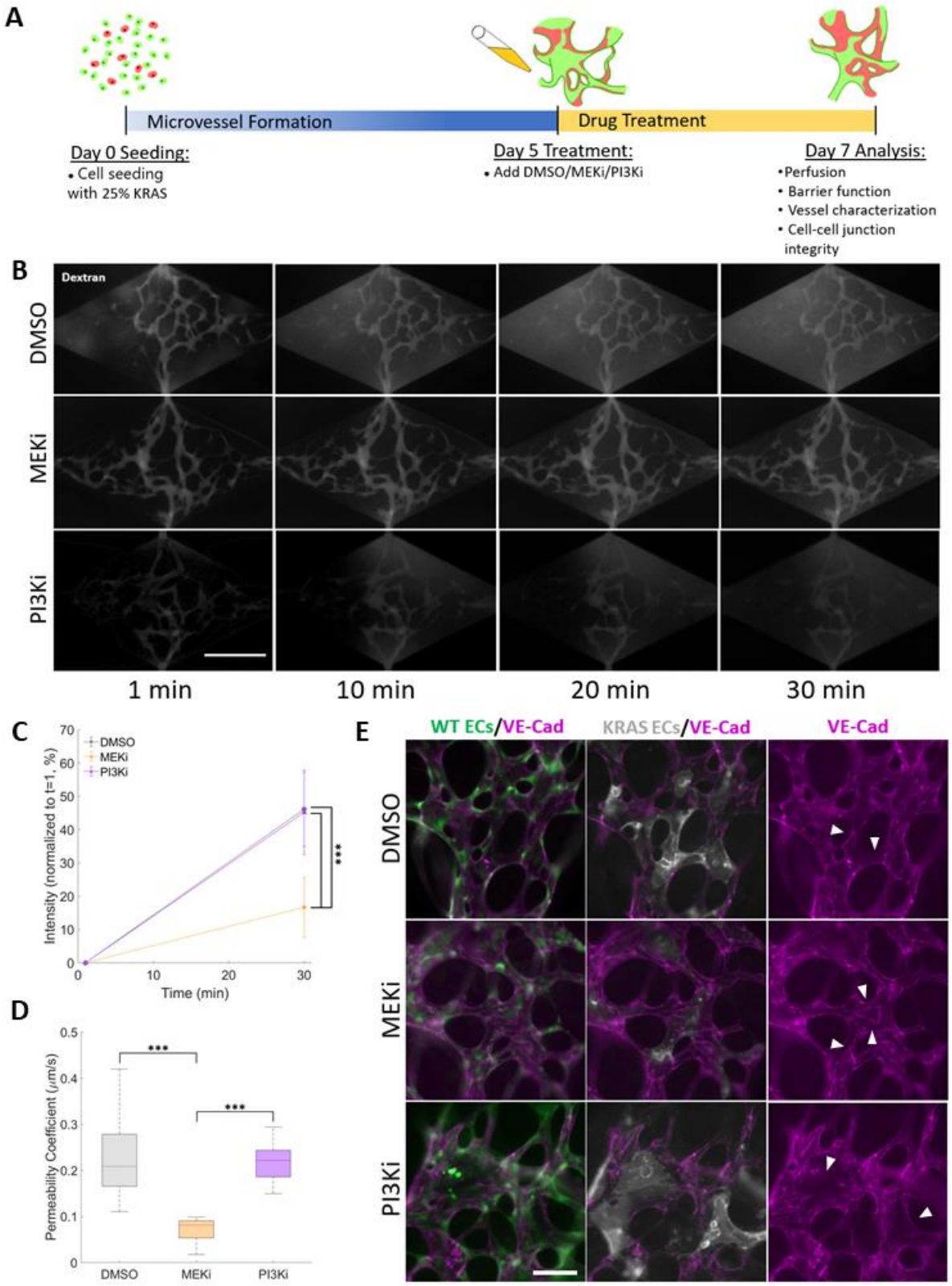

bioRxiv preprint doi: https://doi.org/10.1101/2022.01.20.477166; this version posted January 22, 2022. The copyright holder for this preprint (which was not certified by peer review) is the author/funder. All rights reserved. No reuse allowed without permission.

Figure 5

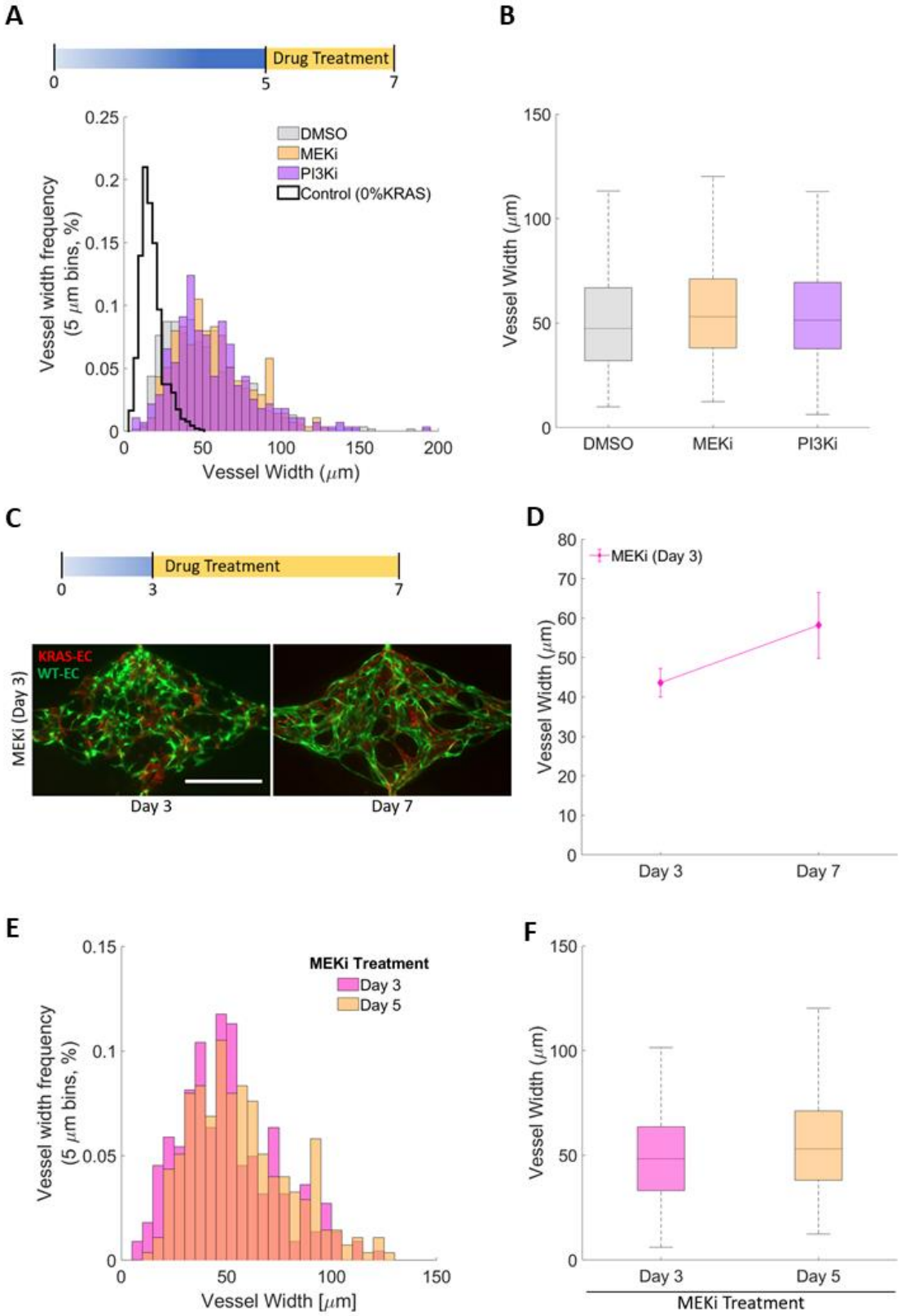

bioRxiv preprint doi: https://doi.org/10.1101/2022.01.20.477166; this version posted January 22, 2022. The copyright holder for this preprint (which was not certified by peer review) is the author/funder. All rights reserved. No reuse allowed without permission.

Supplemental Figures

Supplemental Figure 1

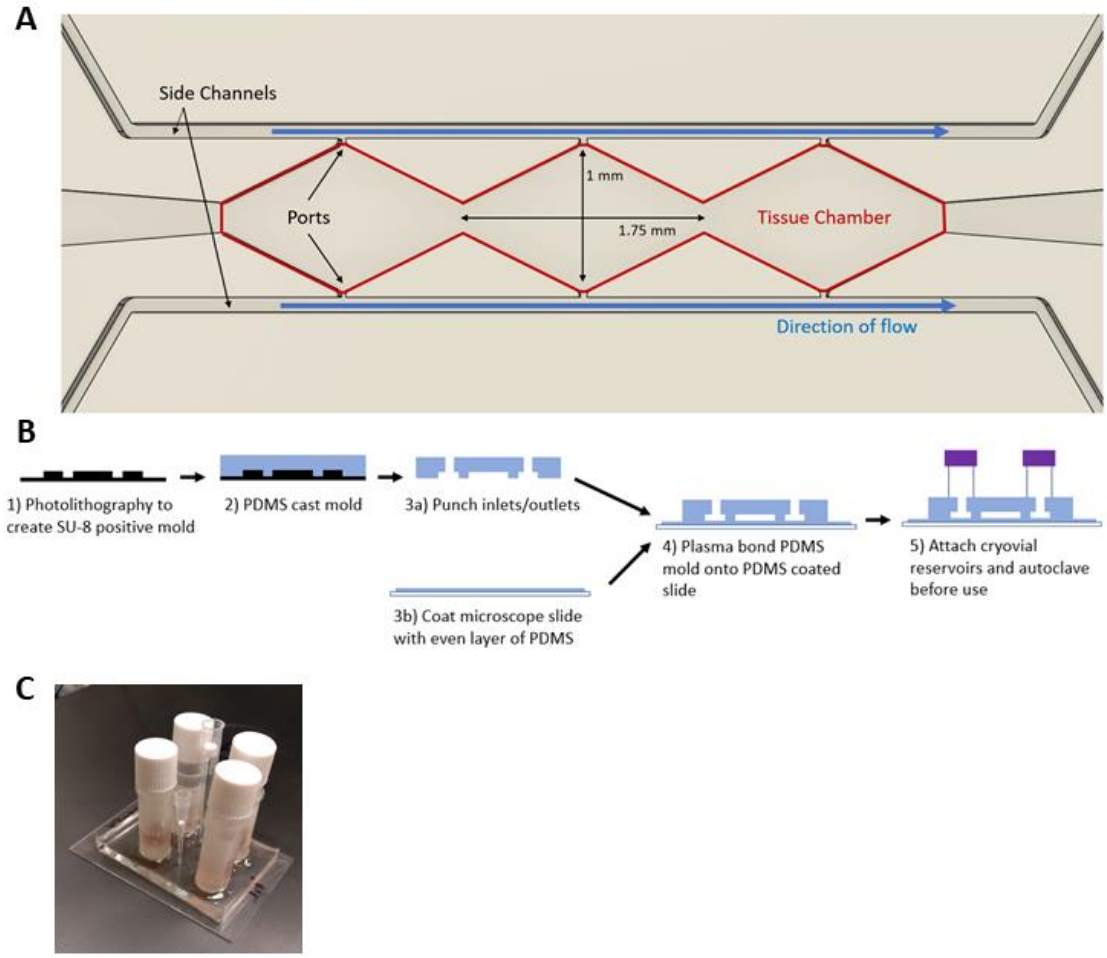

bioRxiv preprint doi: https://doi.org/10.1101/2022.01.20.477166; this version posted January 22, 2022. The copyright holder for this preprint (which was not certified by peer review) is the author/funder. All rights reserved. No reuse allowed without permission.

Supplemental Figure 2

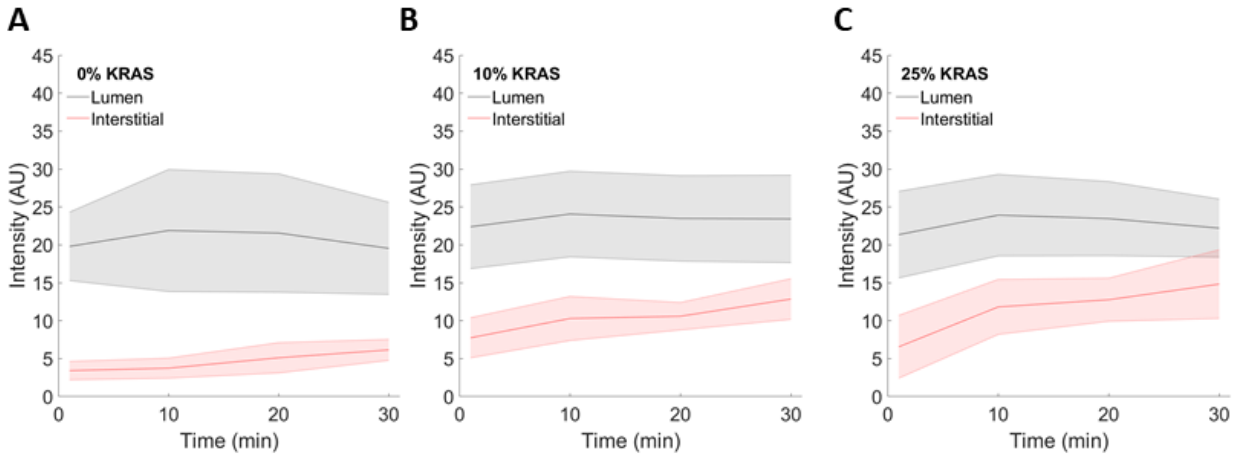

bioRxiv preprint doi: https://doi.org/10.1101/2022.01.20.477166; this version posted January 22, 2022. The copyright holder for this preprint (which was not certified by peer review) is the author/funder. All rights reserved. No reuse allowed without permission.

Manuscript References

1. Solomon RA, Connolly ES. Arteriovenous Malformations of the Brain. *N Engl J Med*. 2017;376(19):1859-1866. doi:10.1056/NEJMra1607407

2. Rutledge WC, Ko NU, Lawton MT, Kim H. Hemorrhage Rates and Risk Factors in the Natural History Course of Brain Arteriovenous Malformations. *Transl Stroke Res*. 2014;5(5):538-542. doi:10.1007/s12975-014-0351-0

3. Al-Shahi R, Warlow C. A systematic review of the frequency and prognosis of arteriovenous malformations of the brain in adults. *Brain J Neurol*. 2001;124(Pt 10):1900-1926. doi:10.1093/brain/124.10.1900

4. Al-Olabi L, Polubothu S, Dowsett K, et al. Mosaic RAS/MAPK variants cause sporadic vascular malformations which respond to targeted therapy. *J Clin Invest*. 2018;128(4):1496-1508. doi:10.1172/JCI98589

5. Nikolaev SI, Vetiska S, Bonilla X, et al. Somatic Activating KRAS Mutations in Arteriovenous Malformations of the Brain. *N Engl J Med*. 2018;378(3):250-261. doi:10.1056/NEJMoa1709449

6. Cheng F, Nussinov R. KRAS Activating Signaling Triggers Arteriovenous Malformations. *Trends Biochem Sci*. 2018;43(7):481-483. doi:10.1016/j.tibs.2018.04.007

7. Fish JE, Flores-Suarez CP, Boudreau E, et al. Somatic Gain of KRAS Function in the Endothelium is Sufficient to Cause Vascular Malformations that Require MEK but not PI3K Signaling. *Circ Res*. Published online June 17, 2020:CIRCRESAHA.119.316500. doi:10.1161/CIRCRESAHA.119.316500

8. Cheng P, Ma L, Shaligram S, et al. Effect of elevation of vascular endothelial growth factor level on exacerbation of hemorrhage in mouse brain arteriovenous malformation. *J Neurosurg*. Published online April 26, 2019:1-8. doi:10.3171/2019.1.JNS183112

9. Walcott BP, Winkler EA, Rouleau GA, Lawton MT. Molecular, Cellular, and Genetic Determinants of Sporadic Brain Arteriovenous Malformations. *Neurosurgery*. 2016;63 Suppl 1:37-42. doi:10.1227/NEU.0000000000001300

10. Fish JE, Wythe JD. The molecular regulation of arteriovenous specification and maintenance. *Dev Dyn Off Publ Am Assoc Anat*. 2015;244(3):391-409. doi:10.1002/dvdy.24252

11. Cunha SI, Magnusson PU, Dejana E, Lampugnani MG. Deregulated TGF-β/BMP Signaling in Vascular Malformations. *Circ Res*. 2017;121(8):981-999. doi:10.1161/CIRCRESAHA.117.309930

12. Atri D, Larrivée B, Eichmann A, Simons M. Endothelial signaling and the molecular basis of arteriovenous malformation. *Cell Mol Life Sci CMLS*. Published online September 28, 2013. doi:10.1007/s00018-013-1475-1

13. Wright R, Järvelin P, Pekonen H, Keränen S, Rauramaa T, Frösen J. Histopathology of brain AVMs part II: inflammation in arteriovenous malformation of the brain. *Acta Neurochir (Wien)*. 2020;162(7):1741-1747. doi:10.1007/s00701-020-04328-3

bioRxiv preprint doi: https://doi.org/10.1101/2022.01.20.477166; this version posted January 22, 2022. The copyright holder for this preprint (which was not certified by peer review) is the author/funder. All rights reserved. No reuse allowed without permission.

14. Winkler EA, Birk H, Burkhardt JK, et al. Reductions in brain pericytes are associated with arteriovenous malformation vascular instability. *J Neurosurg*. 2018;129(6):1464-1474. doi:10.3171/2017.6.JNS17860

15. Murphy PA, Kim TN, Huang L, et al. Constitutively active Notch4 receptor elicits brain arteriovenous malformations through enlargement of capillary-like vessels. *Proc Natl Acad Sci*. 2014;111(50):18007-18012. doi:10.1073/pnas.1415316111

16. Choi EJ, Chen W, Jun K, Arthur HM, Young WL, Su H. Novel Brain Arteriovenous Malformation Mouse Models for Type 1 Hereditary Hemorrhagic Telangiectasia. *PLOS ONE*. 2014;9(2):e88511. doi:10.1371/journal.pone.0088511

17. Milton I, Ouyang D, Allen CJ, et al. Age-Dependent Lethality in Novel Transgenic Mouse Models of Central Nervous System Arteriovenous Malformations. *Stroke*. 2012;43(5):1432-1435. doi:10.1161/STROKEAHA.111.647024

18. Tual-Chalot S, Oh P, Arthur H. Mouse Models of Hereditary Haemorrhagic Telangiectasia: Recent Advances and Future Challenges. *Front Genet*. 2015;6:25. doi:10.3389/fgene.2015.00025

19. Chen W, Sun Z, Han Z, et al. De novo cerebrovascular malformation in the adult mouse after endothelial Alk1 deletion and angiogenic stimulation. *Stroke*. 2014;45(3):900-902. doi:10.1161/STROKEAHA.113.003655

20. Nielsen CM, Huang L, Murphy PA, Lawton MT, Wang RA. Mouse Models of Cerebral Arteriovenous Malformation. *Stroke*. 2016;47(1):293-300. doi:10.1161/STROKEAHA.115.002869

21. Raj JA, Stoodley M. Experimental Animal Models of Arteriovenous Malformation: A Review. *Vet Sci*. 2015;2(2):97-110. doi:10.3390/vetsci2020097

22. Park ES, Kim S, Huang S, et al. Selective Endothelial Hyperactivation of Oncogenic KRAS Induces Brain Arteriovenous Malformations in Mice. *Ann Neurol*. 2021;89(5):926-941. doi:10.1002/ana.26059

23. Sun Z, Kemp SS, Lin PK, Aguera KN, Davis GE. Endothelial k-RasV12 Expression Induces Capillary Deficiency Attributable to Marked Tube Network Expansion Coupled to Reduced Pericytes and Basement Membranes. *Arterioscler Thromb Vasc Biol*. Published online December 9, 2021:ATVBAHA121316798. doi:10.1161/ATVBAHA.121.316798

24. Andrejecsk JW, Hughes CCW. Engineering perfused microvascular networks into microphysiological systems platforms. *Curr Opin Biomed Eng*. 2018;5:74-81. doi:10.1016/j.cobme.2018.02.002

25. Kutys ML, Chen CS. Forces and mechanotransduction in 3D vascular biology. *Curr Opin Cell Biol*. 2016;42:73-79. doi:10.1016/j.ceb.2016.04.011

26. Hu C, Chen Y, Tan MJA, Ren K, Wu H. Microfluidic technologies for vasculature biomimicry. *Analyst*. 2019;144(15):4461-4471. doi:10.1039/C9AN00421A

bioRxiv preprint doi: https://doi.org/10.1101/2022.01.20.477166; this version posted January 22, 2022. The copyright holder for this preprint (which was not certified by peer review) is the author/funder. All rights reserved. No reuse allowed without permission.

27. Whisler JA, Chen MB, Kamm RD. Control of perfusable microvascular network morphology using a multiculture microfluidic system. *Tissue Eng Part C Methods*. 2014;20(7):543-552. doi:10.1089/ten.TEC.2013.0370

28. Wang X, Phan DTT, Zhao D, George SC, Hughes CCW, Lee AP. An on-chip microfluidic pressure regulator that facilitates reproducible loading of cells and hydrogels into microphysiological system platforms. *Lab Chip*. 2016;16(5):868-876. doi:10.1039/C5LC01563D

29. Kosyakova N, Kao DD, Figetakis M, et al. Differential functional roles of fibroblasts and pericytes in the formation of tissue-engineered microvascular networks in vitro. *Npj Regen Med*. 2020;5(1):1. doi:10.1038/s41536-019-0086-3

30. Kim J, Chung M, Kim S, Jo DH, Kim JH, Jeon NL. Engineering of a Biomimetic Pericyte-Covered 3D Microvascular Network. *PloS One*. 2015;10(7):e0133880. doi:10.1371/journal.pone.0133880

31. Jeon JS, Bersini S, Whisler JA, et al. Generation of 3D functional microvascular networks with human mesenchymal stem cells in microfluidic systems. *Integr Biol Quant Biosci Nano Macro*. 2014;6(5):555-563. doi:10.1039/c3ib40267c

32. Wang X, Phan DTT, Sobrino A, George SC, Hughes CCW, Lee AP. Engineering anastomosis between living capillary networks and endothelial cell-lined microfluidic channels. *Lab Chip*. 2016;16(2):282-290. doi:10.1039/C5LC01050K

33. Wan Z, Zhang S, Zhong AX, et al. A robust vasculogenic microfluidic model using human immortalized endothelial cells and Thy1 positive fibroblasts. *Biomaterials*. 2021;276:121032. doi:10.1016/j.biomaterials.2021.121032

34. Phan DTT, Wang X, Craver BM, et al. A vascularized and perfused organ-on-a-chip platform for large-scale drug screening applications. *Lab Chip*. 2017;17(3):511-520. doi:10.1039/C6LC01422D

35. Tzima E, Irani-Tehrani M, Kiosses WB, et al. A mechanosensory complex that mediates the endothelial cell response to fluid shear stress. *Nature*. 2005;437(7057):426-431. doi:10.1038/nature03952

36. Seebach J, Dieterich P, Luo F, et al. Endothelial Barrier Function under Laminar Fluid Shear Stress. *Lab Invest*. 2000;80(12):1819-1831. doi:10.1038/labinvest.3780193

37. Pan S. Molecular Mechanisms Responsible for the Atheroprotective Effects of Laminar Shear Stress. *Antioxid Redox Signal*. 2009;11(7):1669-1682. doi:10.1089/ars.2009.2487

38. Lapinski PE, Doosti A, Salato V, North P, Burrows PE, King PD. Somatic second hit mutation of RASA1 in vascular endothelial cells in capillary malformation-arteriovenous malformation. *Eur J Med Genet*. 2018;61(1):11-16. doi:10.1016/j.ejmg.2017.10.004

39. Chiu JJ, Chien S. Effects of Disturbed Flow on Vascular Endothelium: Pathophysiological Basis and Clinical Perspectives. *Physiol Rev*. 2011;91(1):10.1152/physrev.00047.2009. doi:10.1152/physrev.00047.2009

bioRxiv preprint doi: https://doi.org/10.1101/2022.01.20.477166; this version posted January 22, 2022. The copyright holder for this preprint (which was not certified by peer review) is the author/funder. All rights reserved. No reuse allowed without permission.

40. Storkebaum E, Quaegebeur A, Vikkula M, Carmeliet P. Cerebrovascular disorders: molecular insights and therapeutic opportunities. *Nat Neurosci*. 2011;14(11):1390-1397. doi:10.1038/nn.2947

41. Ryu JY, Kim YH, Lee JS, et al. Oscillatory shear stress promotes angiogenic effects in arteriovenous malformations endothelial cells. *Mol Med*. 2021;27(1):31. doi:10.1186/s10020-021-00291-6

42. Murphy PA, Lu G, Shiah S, Bollen AW, Wang RA. Endothelial Notch signaling is upregulated in human brain arteriovenous malformations and a mouse model of the disease. *Lab Invest*. 2009;89(9):971-982. doi:10.1038/labinvest.2009.62

43. Vernimmen FJAI. Vascular endothelial growth factor blockade: A potential new therapy in the management of cerebral arteriovenous malformations. *J Med Hypotheses Ideas*. 2014;8(2):57-61. doi:10.1016/j.jmhi.2013.10.001

44. Meadows KN, Bryant P, Pumiglia K. Vascular endothelial growth factor induction of the angiogenic phenotype requires Ras activation. *J Biol Chem*. 2001;276(52):49289-49298. doi:10.1074/jbc.M108069200

45. Bentley K, Franco CA, Philippides A, et al. The role of differential VE-cadherin dynamics in cell rearrangement during angiogenesis. *Nat Cell Biol*. 2014;16(4):309-321. doi:10.1038/ncb2926

46. Altalhi W, Sun X, Sivak JM, Husain M, Nunes SS. Diabetes impairs arterio-venous specification in engineered vascular tissues in a perivascular cell recruitment-dependent manner. *Biomaterials*. 2017;119:23-32. doi:10.1016/j.biomaterials.2016.12.003

47. Nunes SS, Greer KA, Stiening CM, et al. Implanted microvessels progress through distinct neovascularization phenotypes. *Microvasc Res*. 2010;79(1):10-20. doi:10.1016/j.mvr.2009.10.001

48. Zhao Y, Adjei AA. The clinical development of MEK inhibitors. *Nat Rev Clin Oncol*. 2014;11(7):385-400. doi:10.1038/nrclinonc.2014.83

49. Pan P, Weinsheimer S, Cooke D, et al. Review of treatment and therapeutic targets in brain arteriovenous malformation. *J Cereb Blood Flow Metab Off J Int Soc Cereb Blood Flow Metab*. 2021;41(12):3141-3156. doi:10.1177/0271678X211026771

50. Cox AD, Der CJ. Ras history. *Small GTPases*. 2010;1(1):2-27. doi:10.4161/sgtp.1.1.12178

51. Priemer DS, Vortmeyer AO, Zhang S, Chang HY, Curless KL, Cheng L. Activating KRAS mutations in arteriovenous malformations of the brain: frequency and clinicopathologic correlation. *Hum Pathol*. 2019;89:33-39. doi:10.1016/j.humpath.2019.04.004

52. Lekwuttikarn R, Lim YH, Admani S, Choate KA, Teng JMC. Genotype-Guided Successful Treatment of an Arteriovenous Malformation in a Child. *JAMA Dermatol*. 2019;155(2):256-257. doi:10.1001/jamadermatol.2018.4653

53. Cooke DL, Frieden IJ, Shimano KA. Angiographic Evidence of Response to Trametinib Therapy for a Spinal Cord Arteriovenous Malformation. *J Vasc Anom*. 2021;2(3):e018. doi:10.1097/JOVA.0000000000000018

bioRxiv preprint doi: https://doi.org/10.1101/2022.01.20.477166; this version posted January 22, 2022. The copyright holder for this preprint (which was not certified by peer review) is the author/funder. All rights reserved. No reuse allowed without permission.

54. Kofler NM, Cuervo H, Uh MK, Murtomäki A, Kitajewski J. Combined deficiency of Notch1 and Notch3 causes pericyte dysfunction, models CADASIL and results in arteriovenous malformations. *Sci Rep*. 2015;5(1):16449. doi:10.1038/srep16449

55. Sun Z, Kemp SS, Lin PK, Aguera KN, Davis GE. Endothelial k-RasV12 Expression Induces Capillary Deficiency Attributable to Marked Tube Network Expansion Coupled to Reduced Pericytes and Basement Membranes. *Arterioscler Thromb Vasc Biol*. Published online December 9, 2021:ATVBAHA121316798. doi:10.1161/ATVBAHA.121.316798

56. Campisi M, Shin Y, Osaki T, Hajal C, Chiono V, Kamm RD. 3D self-organized microvascular model of the human blood-brain barrier with endothelial cells, pericytes and astrocytes. *Biomaterials*. 2018;180:117-129. doi:10.1016/j.biomaterials.2018.07.014

57. Konczyk DJ, Goss JA, Smits PJ, et al. Arteriovenous malformation associated with a HRAS mutation. *Hum Genet*. 2019;138(11-12):1419-1421. doi:10.1007/s00439-019-02072-y

58. Lawton MT, Rutledge WC, Kim H, et al. Brain arteriovenous malformations. *Nat Rev Dis Primer*. 2015;1(1):1-20. doi:10.1038/nrdp.2015.8

59. Pawlikowska L, Nelson J, Guo DE, et al. Association of common candidate variants with vascular malformations and intracranial hemorrhage in hereditary hemorrhagic telangiectasia. *Mol Genet Genomic Med*. 2018;6(3):350-356. doi:10.1002/mgg3.377

60. Davis RB, Pahl K, Datto NC, et al. Notch signaling pathway is a potential therapeutic target for extracranial vascular malformations. *Sci Rep*. 2018;8(1):17987. doi:10.1038/s41598-018-36628-1

61. Couto JA, Huang AY, Konczyk DJ, et al. Somatic MAP2K1 Mutations Are Associated with Extracranial Arteriovenous Malformation. *Am J Hum Genet*. 2017;100(3):546-554. doi:10.1016/j.ajhg.2017.01.018

62. Snellings DA, Hong CC, Ren AA, et al. Cerebral Cavernous Malformation: From Mechanism to Therapy. *Circ Res*. 2021;129(1):195-215. doi:10.1161/CIRCRESAHA.121.318174